Scanning electron microscopy preparation and analysis of the cell cortex ultrastructure

D. Flormann[1], M. Schu[1], E. Terriac[1], M. Koch[1], S. Paschke[2], F. Lautenschläger[1]

[1] Leibniz Institute for New Materials (INM), Saarland University, Saarbrücken 66123, Germany

[2] Department of General and Visceral Surgery, Ulm University, Ulm, 89081, Germany

***Corresponding author: Daniel Flormann**

Campus D2.2

66123 Saarbrücken

Germany

Tel: +49 681 9300 394

Fax: +49 681 9300 223

Email: Daniel.Flormann@web.de

Abstract

The cellular cortex is a 200-nm-thick actin network that lies beneath the cell membrane. It is responsible for the mechanical properties of the cell and is involved in many cellular processes, such as cell migration and interactions with the environment. To develop a clear view of the structure of this meshwork, high resolution imaging is essential, such as electron microscopy. This technique requires complex sample preparation that can lead to artifacts like shrinkage or hole formation. We present a preparation method that reduces artifacts significantly. Here, the final drying step that is typically performed by critical point drying is replaced by hexamethyldisilazane drying. We quantitatively investigated sample integrity after both preparation methods, and show that there are significant advantages of hexamethyldisilazane drying compared to critical point drying. Furthermore, automated analysis of a network is classically performed by thresholding-based software programs, which are sensitive to noise and uneven brightness of images. The here presented analysis that we have developed is based on a vectorial node algorithm. It reproduces all kinds of networks sufficiently to allow derivation of quantitative network-specific parameters, such as mesh hole size. We use this analysis to compare the network structure of cells prepared by these two drying methods, and show that hexamethyldisilazane drying leads to fewer artificial mesh holes compared to critical point drying. We thus present here a significantly improved method to quantitatively investigate the actin cortex of cells, and show that hexamethyldisilazane drying leads to more accurate imaging compared to critical point drying.

Insight Box

The highest resolution for imaging the cellular actin cortex is provided by electron microscopy. Scanning electron microscopy samples require a drying process, usually

achieved by critical point drying, which is critical for the sample integrity. We compare the structural defects in the actin cortex of hTert RPE1 cells after critical point drying and a chemical based method, namely hexamethyldisilazane drying. In order to characterize the actin network, we also developed a new vectorial based tracing software. We bring here new tool, both experimental and analytical, which will help to streamline studies of the actin cortex.

Introduction

The actin cell cortex assembles under the cell membrane with a typical thickness of 200 nm. It is the main determining factor for the cellular mechanical properties. Understanding the structure of this thin dynamic meshwork has attracted great interest in recent years [1, 2], especially under conditions where its adaptation is crucial, such as for mitosis [3], cell migration [4, 5] and differentiation [6].

Given the mesh size of the cortex (<100 nm) [1, 2, 7-9], its structural properties are difficult to address with conventional light microscopy. While some recent studies have produced more accurate representations of this network using super-resolution microscopy [10, 11] and rapid atomic force microscopy (AFM) [8, 12], the main technique applied in such studies remains scanning electron microscopy (SEM). It is possible to extract quantitative data on the superstructure of the cellular cortex from electron micrographs; e.g., the mesh size of the network, and the higher organizational structures, such as bundles of filaments and assembled patterns [13].

Most SEM preparation protocols involve the crucial step of sample drying. The preferred method for this step is critical point drying (CPD), which was introduced by Anderson in 1951 [14]. CPD became an important part in the preparation of biological samples for electron microscopy. The principle of this technique relies on the transition from liquid to vapor phase of CO_2 without any phase transition beyond the critical point [15, 16]. The absence of a brutal phase transition induces a better preservation of thin super-structure within the sample. However, it is a highly invasive method that can influence the shape and structure of biological samples through temperature, pressure, and osmolarity changes, coupled with

relatively high cost due to the special equipment needed [17, 18]. As the structure of the cell cortex is finely regulated by actin nucleators (e.g., the formins and Arp 2/3 [19, 20], actin capping proteins [1], and motors, such as myosin), it is important to be able to reduce drying artifacts and discriminate them from real induced changes in the cortex structures.

An alternative drying method is the use of hexamethyldisilazane (HMDS). This drying method has a negligible influence on the sample temperature and is performed under normal pressure conditions, and it is coupled with moderate costs due to the use of the standard chemical HMDS [18]. In contrast to CPD, the physical background of the mode of action of HMDS drying is poorly understood [21-24]. Empirical studies have shown that HMDS drying leads to similar results to those of CPD under specific biological conditions [18, 21, 25]. Typically, these are studies of relatively large structures and their integrity, or the localization of metallic particles. Consequently, HMDS drying is a widely used method for large structures, while small structures like the actin cortex of cells are commonly investigated using CPD [1, 2, 26]. At the cellular level, both CPD and HMDS drying are known to lead to cell shrinkage [17, 25, 27-30].

The visualized structures need to be analyzed for quantitative measurements. The reproducibility of structural analyses of networks has been addressed using different approaches. The classical thresholding and segmentation approaches are widely available. For example, plug-ins such as DiameterJ are implemented in ImageJ, and allow correct tracing if the threshold used reproduces the network sufficiently well, which is only the case if the network differs strongly from the background [31, 32]. For SEM images of the cellular cortex, the three-dimensional structures of the actin fibers lead to significant variations in the

gray value of single fibers. Therefore, algorithms based on thresholding typically overestimate or/and underestimate the actual network.

To increase the accuracy of the analysis of our imaged networks, we developed a method for network recognition using a vectoral tracing algorithm in combination with (starting) nodes [33, 34]. Such methods are, for example, based on second order Gaussian derivatives of each pixel, to follow high or low pixel intensities, in order to correctly recognize fibers correctly. This powerful technique has already been used successfully by Sato and co-workers [35].

Here, we show that HMDS drying better preserves the structural integrity of the cell cortex than CPD and produces fewer artifacts. Consequently, HMDS drying leads to better reproducibility and reduces time and costs for the preparation of small-scale structures, such as the dense actin network. Additionally, our analysis shows that HMDS drying is more robust than the classical thresholding method, and its flexibility allows its use in many different contexts.

Materials and methods

Cell culture

Immortalized retinal pigmented epithelium (hTERT-RPE1)cells were grown in DMEM/F12 medium supplemented with 10% fetal bovine serum (Thermo Fisher, MA, USA), 1% Glutamax, and 1% PenStrep under 5% CO_2 at 37 °C, in cell culture flasks (Cellstar, Greiner Bio-One, Austria). For fluorescent imaging, RPE1 cells that stably expressed mCherry LifeAct (kind gift from Matthieu Piel, Paris) were used under the same conditions as the RPE1 wild-type cells.

Electron microscopy preparation prior to final drying

The electron microscopy samples were generally prepared following the protocols of Svitkina, Chugh, and others [1, 26, 36, 37]. In more detail, the cells were detached from the culture flasks using trypsin, re-suspended in growth medium, and left to adhere onto glass slides (Thermo Fisher Scientific, MA, USA) for at least 24 h. The cells were then rinsed three times with serum-free Leibovitz medium (Thermo Fisher Scientific, MA, USA). To dissolve the cell membranes and to pre-fix the cellular cortex, two extractions were performed. The first membrane extraction and pre-fixation solution was composed of 0.5% Triton X-100, 0.25% glutaraldehyde, and 10 µM phalloidin in buffer M (50 mM imidazole, pH 6.8, 50 mM KCl, 0.5 mM $MgCl_2$, 0.1 mM EDTA, 1 mM EGTA) and was added to the cells for 5 min. The second extraction was composed of 2% Triton X-100 in 1% CHAPS in milliQ water, and was added to the cells for 5 min, with no rinsing of the cells between the first and second extractions. This step was followed by rinsing the cells three times with buffer M before adding the fixation solution, which contained 2% glutaraldehyde (EM grade; Science Service GmbH, Germany) and 2% paraformaldehyde (EM grade: Science Service GmbH, Germany) in 100 mM sodium cacodylate (pH 7.3) overnight . Then 0.1% aqueous tannic acid was added for 20 min, without prior rinsing. After the removal of the tannic acid, the cells were washed with distilled water three times. Then 0.2% aqueous uranyl acetate (Science Service GmbH, Germany) in distilled water was added. After 20 min, the cells were rinsed three times with distilled water. In order to affect the actin cortex structure, 100 nM Latrunculin A was used for 30 min at 37 °C prior to cell pre-fixation step. Unless otherwise indicated, all chemicals were purchased from Sigma Aldrich.

Afterwards, the samples were ethanol dried using two syringe pumps (with 60-mL syringes). One syringe added ethanol, the second removed the ethanol solutions in order to increase the ethanol concentration continuously to avoid discrete steps. In this manner, 60 mL 50% aqueous ethanol was added over the time course of 1 h, followed by the same procedure with 100% ethanol. In the end, two manual changes (without using the syringe pumps) with 100% ethanol dried over a molecular sieve were used, with an incubation time of 20 min after each exchange.

After the HMDS drying and CPD, the samples were sputtered with a layer of 5-6 nm platinum (coater: Model 681; Gatan, USA).

Hxamethyldisilazane and critical point drying protocols

After dehydration of the samples through the ethanol series, the cells were either dried using HMDS (>98%; Roth, Austria; for HMDS drying to 98%; >99.9%; Sigma Aldrich, Germany; for drying at 100%), or CPD (Quorum K850; UK) (Table 1). In normal conditions, the HMDS drying was performed at room temperature (~23 °C). In order to reproduce the temperature ramps the samples are exposed to during CPD, HMDS drying was also tested with a temperature shift from 4 °C to 37°C by using a fridge and an incubator. Different HMDS protocols, involving different rates of exchanges were tested and are summarized in Table 1. The HMDS10 protocol turned out to be the most efficient one.

Preliminary experiments have been carried out to fine control the CO_2 exchange rates. However, this fine control did not show any significant differences in the results. With the critical point dryer used for the experiments presented here (K850-CPD; Quorum Technologies, UK), ethanol was exchanged for CO_2 following 10 exchange cycles (minimum

50% of the filling level of the chamber). The chamber was then flushed twice with excess CO_2 for 20 min per flush, followed by the final temperature increase to 37 °C. This was accompanied by a pressure increase up to 90 bar. With the temperature kept constant, the pressure was slowly decreased to 1 bar over 40 min.

Imaging

All electron microscopy images were obtained with an environmental surface scanning microscope (Quanta 400; FEI, USA), using high vacuum mode. For nuclei and cells surface measurements, cells were imaged with a fluorescent microscope (Ti Eclipse; Nikon, Japan), equipped with an incubation chamber (37 °C, 5% CO2 in air) for live cell imaging. Nuclei were stained with 50 ng/mL Hoechst, followed by three rinses with phosphate-buffered saline. The nuclei and cell areas, both in the case of electron and fluorescence microscopy were analyzed by thresholding the images in combination with the particle analysis function of ImageJ.

Atomic force microscopy

Cell height was determined by AFM (Nanowizard 3; JPK Instruments, Bruker, USA), used with MLCT type C cantilevers (Bruker, USA). A setpoint force of 2 nN and an approach velocity of 5 µm/s were used. Comparing the contact point on the cell with the contact point of the substrate next to the cell of interest resulted in cell height measurements.

Image analysis by classical thresholding and used parameters

Images were obtained with a scanning electron microscope (Quanta 400; FEI, USA). The images were analyzed using Image J [32] according to the following procedure: to compare the threshold quality directly with the original image a threshold was set manually by

overlaying the original image with the threshold image. The threshold was chosen in such a way that small mesh holes were not discernable (diameter, <30 nm), as they were not required for the next step of the analysis. At the same time, the big mesh holes were outlined precisely (diameter, >50 nm). In the next step, the *analyze particle* tool was set to only analyze the particles with diameters ≥110 nm (calculated via the areas). According to previous studies [2], the diameters of the mesh hole size of different cell lines was assumed to be <100 nm. Consequently, a threshold of 110 nm includes the meshes of the expected diameters plus a certain standard deviation. Therefore, every mesh hole size >110 nm that was then collected by setting this diameter threshold was assumed to be an artefact that had resulted from the electron microscopy preparation procedure. Additionally, almost all mesh holes >110 nm showed broken filaments pointing to the inside of the holes. This encourages the definition of artificial mesh holes as sample preparation artifacts.

Image analysis using home-made tracing software

The aim of our algorithm is to trace fibers on a grayscale image to increase the precision compared to classical thresholding. This was realized by populating the image with a defined number of starting nodes on the fibers. A circle was taken around each node. An algorithm defined where the fibers were localized on the circle using the second order derivative of the Hessian matrix (see Supplementary Information). At this location, it set a second node that was connected to the first one. This procedure was performed for every node until the whole network was traced. In this way, each node can be connected to an arbitrary number of other nodes, which allows the branching of the traced network and the formation of closed loops.

This procedure led to several potential output parameters, such as the total length of the traced network (respectively, fibers), the branching frequency, and the mesh hole sizes of the

network. The mesh hole size is obtained by realizing closed loops without nodes insight of the loops. In dense networks, almost all of the fibers are parts of closed loops. The traced fibers that are not parts of the closed loops are often at the edges of such images, as the fibers closing the loop lie outside the image.

Details of the tracing algorithm (SI)

Before the image convolution by our algorithm, the image brightness is rescaled to be in-between 0 and 255 (greyscale). To compute the smoothed second-order derivatives of the image brightness, the tracing algorithm works on the basis of the Hessian of the Gaussian transform. The convolution with the three second-order derivatives of the Gaussian transform yields to the Hessian matrix for each pixel. Using the Hessian matrix, the directional second-order derivative for any pixel and any direction can be computed easily. Generally, negative second-order derivatives with large absolute values indicate the presence of a fiber. This fiber travels perpendicular to the direction of this directional second-order derivative. An automatic function sets several starting nodes. From these nodes, the algorithm traces the whole network without multiple tracing of the fibers. The algorithm itself is available here: https://github.com/SRaent/Actin.

Results

HMDS drying *versus* CPD

To compare the final drying methods during the electron microscopy preparation, cells were prepared as described above. Since the preparation methods prior to drying are similar, the first steps were done such as no sample was attributed a drying method *a priori*. During CPD

the cells undergo a temperature change from room temperature down to <10 °C, and then up to 37 °C or higher. To find out if this temperature shift influenced the preparation artefacts, the HMDS drying was performed both at room temperature (~23 °C) and with temperature changes analogous to the CPD, as 4 °C to 37 °C. Representative images are shown in Figure 1 at different magnifications (low, medium and high magnification being respresented on the top, middle and bottom line respectively). In the medium magnification images (Fig. 1, middle panels), it is already possible to see that there are fewer 'cracks' (holes) around the nucleus of the standard HMDS dried sample (i.e., at room temperature), compared to HMDS drying at 4/37 °C and CPD. The highest magnification images (Fig. 1, bottom panels; edge length, 3.14 µm) show the periphery area (i.e., between the nucleus and the edge of the cell). Eye inspection of such representative images , as well as thorough quantification as depicted in Fig 2(b) and (c), indicated that CPD resulted in more and larger artificial mesh holes (AMHs; defined below) than HMDS drying, both with and without the temperature shift. Nonetheless, for all of these preparation protocols, there were cells that were in good conditions (i.e., very few holes, if at all) and in bad condition (i.e., with many holes). Therefore, we carried out quantitative analysis of randomly chosen cells.

Artificial mesh holes were defined as holes >110 nm in diameter, as proposed by Chugh and co-workers [2]. The diameter of the mesh holes was derived from the measured perimeter of each hole assuming circular mesh holes for the diameter calculation. To quantify these AMHs, classical thresholding was used, as well as our algorithm. As both methods provided similar data for AMHs >110 nm in diameter, only data from our algorithm are shown in Fig 2. In this method, any mesh holes <110 nm in diameter were not taken into account. A representative image of AMHs of larger diameter is given in Figure 2a for the HMDS drying. The analysis of the diameters and AMH area fractions for all three conditions (HMDS,

HMDS 4/37 °C, CPD) are shown in Figure 2b, c. There are no significant differences between the AMH diameters for HMDS drying at room temperature and at 4/37 °C, which indicates that temperature has little influence at this preparation step. The AMH diameter for HMDS ranged from 300 nm to 500 nm. In contrast, the AMH diameter distribution for CPD lied between 400 nm and 800 nm and was statistically different to the one obtained for HMDS drying method ($p < 0.001$). At the same time, the area fraction of the AMHs, in terms of the proportion of AMH area compared to the total image area, was not significantly different for HMDS and HMDS 4/37 °C, averaging between 2% to 25% for both conditions. In contrast, the area fraction of the AMHs for CPD was significantly higher ($p < 0.001$), representing a fraction between 10% and 50% of the image area (Fig. 2c). Of note, the temperature decrease as a result of the HMDS evaporation at room temperature was measured to be less than 2 °C (data not shown). Since we did not show an influence of the temperature cycles during HMDS drying at 4/37 °C, these data lead to the conclusion that the AMHs cannot be solely attributed to the temperature cycles during CPD.

Moreover, the exchange concentration and the rates from 100% ethanol to 100% HMDS significantly influenced the AMH diameter measurements. There were no differences in the AMH diameters between the HMDS1 and HMDS10 protocols (see Table 1), as shown in Figure 2d. In contrast, the HMDS25 and HMDS50 protocols (see Table 1) lead to significantly larger AMHs than for the HMDS1 and HMDS10 protocols. Due to practicability, we decided to use the HMDS10 protocol for all of the following presented experiments.

Correlation between artificial mesh holes around the nuclei and at the cell periphery

Artificial mesh holes close to the nuclei can be very large compared to AMHs at the cell periphery. The AMH sizes within a 2 µm large ring around the nuclei were compared to AMHs at the periphery (defined as the area between the outer part of the 2µm ring and the cell edge, see Figure 3b). Figure 3a shows the size distribution of AMHs >110 nm around the nucleus for both HMDS drying and CPD. AMHs at the periphery and AMHs close to the nuclei are clearly correlated (Fig. 3c, d). For both HMDS drying and CPD, the total and the mean size of the AMHs at the periphery increased with the AMH size around the nuclei. This correlation between AMHs around the nuclei and at the periphery is eventually helpful to rapidly define the quality of SEM-samples. Rapid imaging of the perinuclear region (2µm ring) is enough to determine whether a user should spend time on one particular sample to focus on and to optimize the parameters for the imaging at the periphery.

Origin of artificial mesh holes around nuclei

In most cases AMHs were seen around the nuclei, as it was already shown in other studies [1, 2, 26, 36, 37]. However, the origin of these AMHs has, to the best of our knowledge, not been investigated to date. As these AMHs are around the nuclei, our hypothesis was that these AMHs appear during strong shrinkage of the nuclei compared to the rest of the cell. Therefore, we measured the nuclei and cell sizes for living and fixed cells by fluorescent microscopy, as well as after the final drying with either HMDS drying or CPD by electron microscopy. Additionally, to determine whether the cell shrinkage also affects the height of the cells, cell height above the nucleus and at the cell periphery was probed by AFM. The sole fixation of cells with 2% paraformaldehyde and 2% glutaraldehyde in 0.1M cacodylate buffer had no influence on the cell area, as shown in Figure 4a. In contrast, the nuclear area was significantly reduced after HMDS drying and CPD compared to living and fixed cells. We also observed that the nuclear area was significantly larger after HMDS drying, compared to

cells which had been dried by CPD (Fig. 4b). Consequently, we concluded that the AMHs around the nuclei are caused by significantly greater shrinkage of the nuclei compared to the periphery of the cell. The smaller shrinkage of the nuclei induced by the HMDS procedure explains why samples dried with this protocol have, on average, fewer and smaller AMHs. As such, HMDS drying is less invasive and alters the cellular morphology less than CPD.

However, both methods resulted in significant shrinkage in cell height during the fixation step. Additionally, decrease in cell height was also measured during the final drying step for both of the drying methods (Fig. 4c, d). While the nuclear height was reduced more with HMDS drying, the periphery height showed no significant reductions in height comparing HMDS drying and CPD (Fig. 4c, d). This leads to the conclusion that the significant shrinkage of the nuclei but no shrinkage of the cell parallel to the surface is the main driver for AMHs at the cell periphery.

The fixation and drying influence on the cells is illustrated in Fig. 4e.

New algorithm for fiber detection and mesh hole size determination of the cellular actin

We developed an algorithm to trace the cortex structures in these SEM images. This tracing identifies cortical structures more accurately than the classical thresholding method, which leads always to overestimation or underestimation of the actual network. An exemplary tracing for wild-type RPE1-cells is shown in Figure 5 (top row images) and compared to Latrunculin A treated cells, a condition in which the actin polymerization is partially inhibited, leading to bigger mesh holes (bottom row images). By analyzing all mesh holes present in the cortex, we found a mesh hole size of 64 +/- 14 nm (mean +/- SD) for RPE1-wt

cells and 68.4 +/- 28 nm (mean +/- SD) for Latrunculin A treated cells (Fig. 5d). In addition, the number of branches/nodes decreases when cells were treated with Latrunculin A (Fig. 5h).

To quantify the quality of our tracing algorithm, we measured the maximum density of the fibers that are traceable within an acceptable error (10% SD). To do so, we digitally created an orthogonal grid of white fibers on a black background. For this network we increased the number of fibers, and thereby the density of fibers, from 26% coverage with white pixels (74% black pixels) up to 92% with white pixels (8% black pixels), as illustrated in Fig. 6a. The relative root square deviations were taken for the comparisons of the known mesh-hole sizes *versus* the measured mesh-hole sizes. As shown in Figure 6b, the expected mesh hole size is in good agreement with the measured mesh hole size analyzed by our algorithm. We conclude that our algorithm allows a relatively accurate description of porous and dense networks, with up to 92% coverage of the fibers.

Contrary to our self-generated grid, electron micrographs always display a certain level of noise. Consequently, we investigated the maximum signal to noise ratio that our program can handle while giving a good measurement of mesh hole sizes. Therefore, digital noise was added to the grid created with 73% black pixels. An example of the tracing results for these images is given in Fig. 7a. Analysis of the relative root square deviations indicated that a signal-to-noise ratio of 0,83 dB is still traceable, within an error of below 10% (Fig. 7b). As comparison the signal-to-noise ratio of the electron microscopy images of the cortex are in the range between 5 and 15 dB.

Variety of applications of the tracing algorithm

While we developed our algorithm in order to quantify actin cortex meshes from electron micrographs, it still can be adapted to the recognition of different fiber-like structure imaged by different techniques. To demonstrate this, several images of random objects that included fiber-like networks were taken with a camera at different magnification and analyzed with our algorithm: spaghetti, a three-dimensional tunnel painted on a wall, the structure of leather, a line drawing of a person, human leg hairs, and handwriting (Fig. 8). These examples demonstrate that this software can be used for analysis of a wide variety of network images, which proofes it as a powerful tool for all network quantification across many applications.

Discussion

Little is known about the precise origin of AMHs. There are several explanations possible that can define this process for the artefacts observed. One explanation indicates that this might arise from water or ethanol remaining within the sample before the final drying process. During CPD neither water nor ethanol traces would reach their critical point (374 °C at 221 bar for water and 241 °C, at 60 bar for CO2), thus the transition from liquid to gas of either compound would be accompanied with a sudden change of density leading to potential fractures of the thin structures of the sample. In the case of HMDS drying, the HMDS itself combines both the low surface tension of ethanol (18mN/m for HMDS and 22 mN/m for ethanol) and the low vapor pressure of water (23 mmHg for HMDS; 17,5 mmHg for water). These properties translate into a lower rate of drying and the liquid-gas transition induces less mechanical stress on the microstructures. The potential crosslinking properties of HMDS towards biological sample have also been suggested as a reason of observing less shrinkage in biological tissues during drying [24]. Nonetheless, HMDS drying does not involve critical

point, contrary to CPD, and thus the liquid to gas transition will always be accompanied by changes in densities.

In addition, local shrinkage of samples was shown during HMDS drying and CPD up to 30% for large scales, such as in tissues [14, 15, 18]. This shrinkage will always lead to local tensions in the sample, which can potentially affect microstructures such as the actin cortex.

A further effect might arise from the exchanges of solutions during the preparation. The osmolality of these solutions can vary from 10 to 50 mOsmol/L (for MilliQ water) to over 300 mOsmol/L (for medium, Leibovitz, first extraction solution), and up to 700 mOsmol/L (for the fixation solution). We aimed to minimize these effects by the successive and slow addition of each solution in order to reduce the osmotic shock. While this effect was reduced, it can still not be completely excluded.

Finally, CPD has two additional aspects that are not part of HMDS drying. First, the pressure during CPD varies between 1 bar to 80 bar, or even higher. In principle, this should not have a significant influence on the sample, as long as there are no air-filled cavities. While we haven't noticed such cavities, one cannot fully discard the potential presence of nanometer size air-pocket. The compression of ethanol during the pressure increase up to 50 to 60 bar at the beginning of CPD is in the range of a 0.5% volume compression, and as such, the impact on the sample should be neglectable. However, the degassing of CO_2 to reduce the pressure to atmospheric pressure is a particularly delicate step. If this happens too quickly, the gas can expand and potentially rupture the ultrastructure, which will lead to AMHs. The second aspect is the wide temperature change during CPD, from ~5 °C to 40 °C, while HMDS drying is carried out at room temperature, and only shows a temperature decrease of 2 °C below

room temperature at maximum. However, simulation of the temperature difference of CPD for HMDS drying showed that the temperature had no significant effects on AMH sizes.

All in all, while it would be mostly impossible to avoid AMH in HMDS drying due to local surface tension, the kinetic of the reaction makes those AMH smaller and fewer in number and sample preparation is less sensitive to traces of water or ethanol as well as the rate of sample degassing.

Conclusions

To examine the intact cellular cortex using SEM, the preparation follows four essential steps: membrane removal; fixation; dehydration; and drying. This process often leads to artifacts, and these appear to arise during the final drying process, which is commonly performed as CPD [1, 2, 26, 36, 37]. HMDS drying represents an improved alternative to CPD. We have shown here that both of these drying methods lead to artifacts, but that for HMDS drying, the AMHs are significantly smaller than for CPD.

Moreover, we have shown that the sizes of the AMHs around the nuclei and at the periphery of cells are correlated. Our explanation for this correlation relates to the shrinkage of the nuclei in three dimensions, coupled with no change in the size of the outer edge of the cell during the preparation. We postulate that this collapse of the cellular cortex around the nuclei will lead to increased tension towards the periphery, and therefore AMHs appear to reduce this local tension.

To accurately analyze such network structures as the cellular cortex, we used a vectoral tracing algorithm that accurately traces a wide diversity of networks. These networks can be accurately traced for up to 92% fiber coverage and a signal-to-noise ratio of 0,83, assuming a maximum error of 10%. The algorithm itself is limited to white fibers of approximately uniform thickness on a dark background.

Finally, we were able to measure the average mesh hole diameter of the actin cortex of RPE1 wild-type cells and found this size to approximately be 64 nm. After actin polymerization disturbance by using LatrunculinA, the mesh hole size of the cortex increased significantly by almost 7% confirming that the structural properties of the cell cortex is directly linked ot the actin dynamic. Altogether we propose here a combination of technical and analytical tools and their limitations. These tools will be of great help to improve the rate of success as well as the standardization of the measurement of actin cell cortex in the future.

Conflicts of Interest

The authors declare that they have no conflicts of interest regarding the publication of this work.

Acknowledgments

This work was supported by: Leibniz Institut für neue Materialien (INM), Saarland university Saarbrücken, Germany [CRC 1027 (A9)] and Ulm university, Ulm, Germany [CRC 1149 (A6)]

References

1. Chugh, P., et al., *Actin cortex architecture regulates cell surface tension.* Nat Cell Biol, 2017. **19**(6): p. 689-697.
2. Chugh, P. and E.K. Paluch, *The actin cortex at a glance.* J Cell Sci, 2018. **131**(14).
3. Fischer-Friedrich, E., et al., *Quantification of surface tension and internal pressure generated by single mitotic cells.* Sci Rep, 2014. **4**: p. 6213.
4. Yamaguchi, H. and J. Condeelis, *Regulation of the actin cytoskeleton in cancer cell migration and invasion.* Biochim Biophys Acta, 2007. **1773**(5): p. 642-52.
5. Le Clainche, C. and M.F. Carlier, *Regulation of actin assembly associated with protrusion and adhesion in cell migration.* Physiol Rev, 2008. **88**(2): p. 489-513.
6. Maloney, J.M., et al., *Mesenchymal stem cell mechanics from the attached to the suspended state.* Biophys J, 2010. **99**(8): p. 2479-87.
7. Charras, G.T., et al., *Life and times of a cellular bleb.* Biophys J, 2008. **94**(5): p. 1836-53.
8. Kronlage, C., et al., *Feeling for Filaments: Quantification of the Cortical Actin Web in Live Vascular Endothelium.* Biophys J, 2015. **109**(4): p. 687-98.
9. Eghiaian, F., A. Rigato, and S. Scheuring, *Structural, mechanical, and dynamical variability of the actin cortex in living cells.* Biophys J, 2015. **108**(6): p. 1330-1340.
10. Fritzsche, M., et al., *Cytoskeletal actin dynamics shape a ramifying actin network underpinning immunological synapse formation.* Sci Adv, 2017. **3**(6): p. e1603032.
11. Xu, K., H.P. Babcock, and X. Zhuang, *Dual-objective STORM reveals three-dimensional filament organization in the actin cytoskeleton.* Nat Methods, 2012. **9**(2): p. 185-8.
12. Yoshida, A., et al., *Probing in vivo dynamics of mitochondria and cortical actin networks using high-speed atomic force/fluorescence microscopy.* Genes Cells, 2015. **20**(2): p. 85-94.
13. Fritzsche, M., et al., *Self-organizing actin patterns shape membrane architecture but not cell mechanics.* Nat Commun, 2017. **8**: p. 14347.

14. ANDERSON, T.F., *TECHNIQUES FOR THE PRESERVAATION OF THREE-DIMENSIONAL STRUCTURE IN PREPARING SPECIMENS FOR THE ELECTRON MICROSCOPE*.* 1951. **13**(4 Series II): p. 130-134.

15. Ambrosetti, A. and P.H. Rabinowitz, *Dual variational methods in critical point theory and applications.* Journal of Functional Analysis, 1973. **14**(4): p. 349-381.

16. Horridge, G.A. and S.L. Tamm, *Critical Point Drying for Scanning Electron Microscopic Sthdy of Ciliary Motion.* Science, 1969. **163**: p. 817-818.

17. Boyde, A., F. Franc, and E. Maconnachie, *Measurements of critical point shrinkage of glutaraldehyde fixed mouse liver.* Scanning, 1981. **4**: p. 69-82.

18. Araujo, J.C., et al., *Comparison of hexamethyldisilazane and critical point drying treatments for SEM analysis of anaerobic biofilms and granular sludge.* Microscopy, 2003. **52**(4): p. 429-433.

19. Bovellan, M., et al., *Cellular control of cortical actin nucleation.* Curr Biol, 2014. **24**(14): p. 1628-1635.

20. Rottner, K., et al., *Actin assembly mechanisms at a glance.* J Cell Sci, 2017. **130**(20): p. 3427-3435.

21. Nation, J.L., *A New Method Using Hexamethyldisilazane for Preparation of Soft Insect Tissues for Scanning Electron Microscopy.* Stain Technology, 1983. **58**(6): p. 347-351.

22. Heegaard, S., O.A. Jensen, and J.U. Prause, *Hexamethyldisilazane in Preparation of Retinal Tissue for Scanning Electron Microscopy.* Ophthalmic Research, 1986. **18**(4): p. 203-208.

23. Fischer, E.R., et al., *Scanning electron microscopy.* Current protocols in microbiology, 2012. **Chapter 2**: p. Unit2B.2-2B.2.

24. Lee, J.T.Y. and K.L. Chow, *SEM sample preparation for cells on 3D scaffolds by freeze-drying and HMDS.* 2012. **34**(1): p. 12-25.

25. Braet, F., R. De Zanger, and E. Wisse, *Drying cells for SEM, AFM and TEM by hexamethyldisilazane: a study on hepatic endothelial cells.* J Microsc, 1997. **186**(Pt 1): p. 84-7.

26. Svitkina, T.M., *Platinum replica electron microscopy: Imaging the cytoskeleton globally and locally.* Int J Biochem Cell Biol, 2017. **86**: p. 37-41.

27. Katsen-Globa, A., et al., *Study of SEM preparation artefacts with correlative microscopy: Cell shrinkage of adherent cells by HMDS-drying.* Scanning, 2016. **38**(6): p. 625-633.

28. Jusman, Y., S.C. Ng, and N.A. Abu Osman, *Investigation of CPD and HMDS sample preparation techniques for cervical cells in developing computer-aided screening system based on FE-SEM/EDX.* ScientificWorldJournal, 2014. **2014**: p. 289817.

29. Schutten, W.H. and D.L. Van Horn, *Corneal endothelial cell shrinkage after critical point drying.* Annals of ophthalmology, 1980. **12**(10): p. 1165-1167.

30. Gusnard, D. and R.H. Kirschner, *Cell and organelle shrinkage during preparation for scanning electron microscopy: effects of fixation, dehydration and critical point drying.* J Microsc, 1977. **110**(1): p. 51-7.

31. Hotaling, N.A., et al., *DiameterJ: A validated open source nanofiber diameter measurement tool.* Biomaterials, 2015. **61**: p. 327-38.

32. Schindelin, J., et al., *The ImageJ ecosystem: An open platform for biomedical image analysis.* Mol Reprod Dev, 2015. **82**(7-8): p. 518-29.

33. Meijering, E., et al., *Design and validation of a tool for neurite tracing and analysis in fluorescence microscopy images.* Cytometry A, 2004. **58**(2): p. 167-76.

34. Winkler, C., et al., *Actin filament tracking in electron tomograms of negatively stained lamellipodia using the localized radon transform.* J Struct Biol, 2012. **178**(1): p. 19-28.

35. Sato, Y., et al., *Three-dimensional multi-scale line filter for segmentation and visualization of curvilinear structures in medical images.* Medical Image Analysis, 1998. **2**(2): p. 143-168.

36. Svitkina, T.M., Borisy, G.G., *Electron microscopy of the cytoskeleton of cultured cells.* Recent Advances in Microcopy of Cells, Tissues and Organs, 1997: p. 93-100.

37. Svitkina, T.M., A.B. Verkhovsky, and G.G. Borisy, *Improved procedures for electron microscopic visualization of the cytoskeleton of cultured cells.* J Struct Biol, 1995. **115**(3): p. 290-303.

Table 1. Hexamethyldisilazane drying protocols, carried out at room temperature (~23 °C), 4 °C, and 37 °C.

Protocol code	**Primary HMDS procedure**			**Secondary HMDS procedure**		
	Step size (%)	**Incubation time (min)**	**Total steps**	**Wash**	**Wash time**	**Completion**
HMDS1	1	0.5	100	100%	20 min, ×2	Evaporation
HMDS10	10	5	10	100%	20 min, ×2	Evaporation
HMDS25	25	5	4	100%	20 min, ×2	Evaporation
HMDS50	50	5	2	98%	10 min, ×1	Evaporation

Figure legends

Figure 1: Scanning electron microscopy images of hmds drying and CPD. Representative scanning electron microscopy images for three different conditions for the final preparation step: HMDS dried (left column), HMDS dried at 4/37 °C (middle column), and critical point dried (right column). Top: Whole cell images, indicating (blue boxes) the sensitive area around the nucleus magnified in the middle images. Bottom: magnification of the periphery (area between nucleus and cell edge) Scale bars: 20 µm (top row); 5 µm (middle row); 1 µm (bottom row).

Figure 2: AMH analysis upon different preparation procedures. **(a)** Analysis of mesh holes overlaid on an original image. The sample was HMDS dried at room temperature (see Fig. 1, bottom left). Scale bar: 1 µm. **(b)** Mean diameter of artificial mesh holes (AMH) calculated via the perimeters for around 30 images (i.e., 30 cells). **(c)** Total area fraction of the analyzed areas based on whole image size. **(d)** AMH diameters for different HMDS samples (see Table 1). * $p < 0.05$, ** $p < 0.01$, *** $p < 0.001$, **** $p < 0.0001$, n.s. not significant (t-tests).

Figure 3: Comparison of AMH close to the nucleus and in periphery. (a) Representative image of a cell nucleus (outlined in green) of a cell prepared by CPD. The surrounding artificial mesh holes are indicated in red, to a 2 µm distance from the edge of the nucleus. Scale bar: 10 µm. **(b)** Representative image of a cell prepared by hmds drying. Green outline refers to the nucleus, red outline refers to the 2 µm distance from the edge of the nucleus. The area defined as periphery lays between the red and black outline. Scale bar: 10 µm **(c, d)** Comparisons of total AMH areas around the nuclei (e.g., red outlines in (a)) with the total and

averaged areas of the cell periphery (area between red and black outline in (b)). Lines, linear approximations. Squares, CPD; circles, hmds10.

Figure 4: Influence of fixation and final drying. Geometry changes of the cell during preparation for scanning electron microscopy. **(a, b)** Measurements from scanning electron microscopy of cell areas (a) and nucleus areas (b) by fluorescent microscopy of these living and fixed cells. **(c, e)** Measurements from atomic force microscopy of the nucleus heights (c) and cell periphery heights (d). **(e)** Illustration of the four conditions investigated (i.e., living and fixed cells, and after HMDS drying and CPD). * $p < 0.05$, *** $p < 0.001$, n.s. not significant (t-tests).

Figure 5: Mesh hole size analysis. Representative images of the cellular cortex of adhered wild-type RPE1-cells **(a)** and adhered RPE1-cells treated with 100 nM Latrunculin A for 30 min **(e)** with networks traced using our tracing algorithm **(b, f)** and the magnification of the blue rectangle in **(c, g)**. The analysis of the mesh hole areas below 110 nm in diameter **(d)** and the analysis of the number of junctions/nodes per fiber length **(h)** are compared for the wild-type RPE1-cells (control) and Latrunculin A treated cells. Red tracing lines, closed loops; green tracing lines, open loops. Scale bars: 1 µm for (a, b, d, e); 100 nm for (c, f).

Figure 6: Accuracy of the tracing algorithm. **(a, b)** Created quadratic black mesh holes with increasing mesh hole size (as indicated) as designed (a) and traced using our software in (b). **(c)** Known mesh hole size *versus* the mesh hole size calculated via the tracing algorithm with a linear approximation.

Figure 7: Influence of noise on tracing accuracy. **(a)** Artificial mesh holes (73% black pixels) as designed with noise addition (left column) and as traced using our algorithm (right column), with signal-to-noise ratios as indicated. Red tracing lines, closed loops; blue tracing lines, open loops. **(b)** The measured mesh holes shown in (a) were compared without and with noise additions, assuming no tracing as 100% standard deviation, to provide relationship shown between normalized standard deviation and signal-to-noise ratio. At 0,83 dB and higher, the normalized standard deviation is <10%, so a signal-to-noise ratio ≥0,83 dB is recommended for using our algorithm.

Figure 8: General examples of network tracing with our algorithm. Images of examples of tracing of different kinds of networks using our algorithm. All images were color modified for bright 'fibers' and dark backgrounds. Left, original image; right, traced image. The images shown and traced are a dense network of spaghetti **(a)**, a porous network of spaghetti **(b)**, a three-dimensional tunnel painted on a wall **(c)**, the structure of leather **(d)**, a line drawing of a person **(e)**, human leg hairs **(f)**, and handwriting **(g)**. Red tracing lines, closed loops, blue tracing lines, open loops.

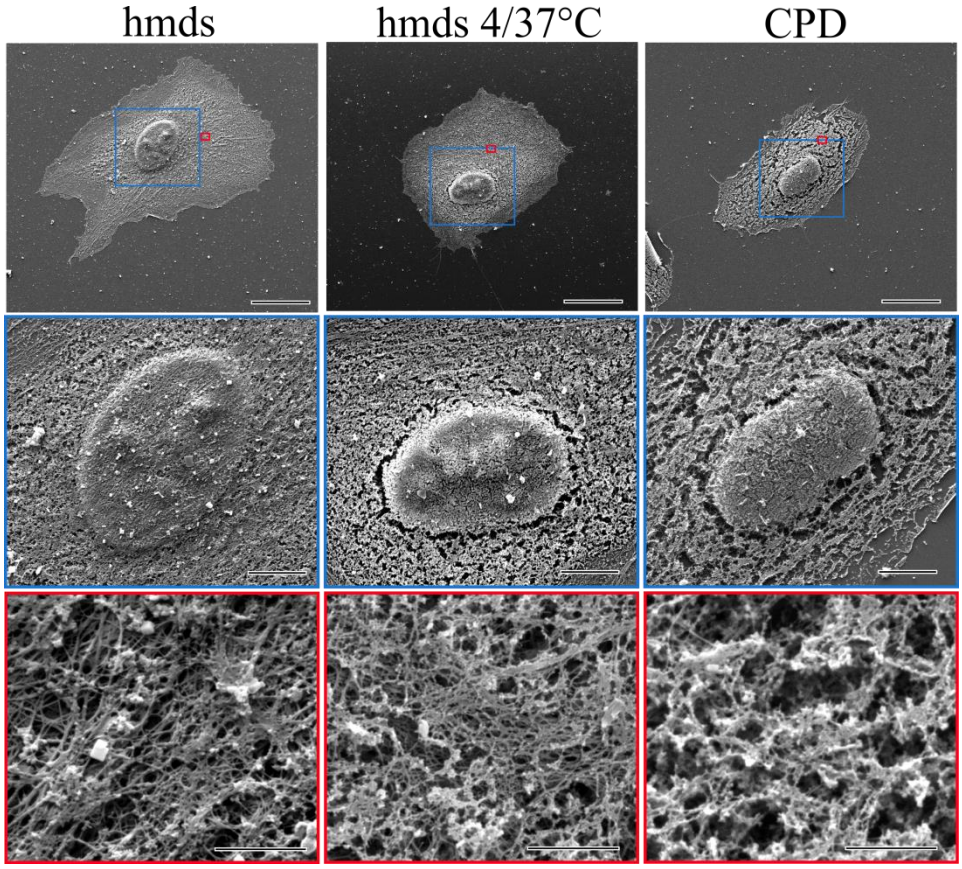

Figure 1

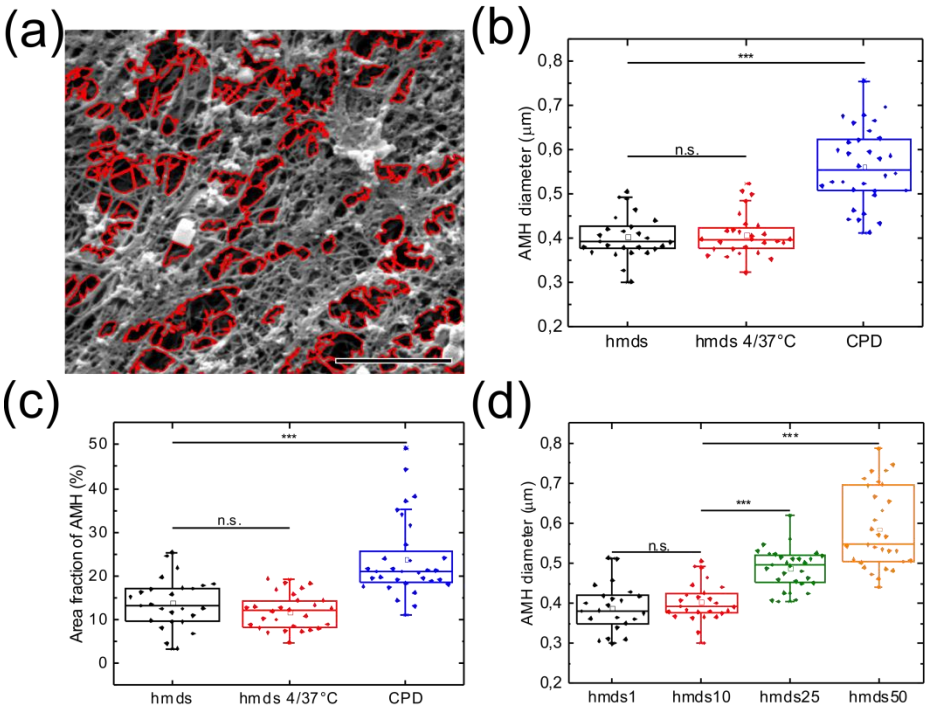
(a)
(b)
AMH diameter (µm)
0,8
0,7
0,6
0,5
0,4
0,3
0,2
***
n.s.
hmds
hmds 4/37°C
CPD
(c)
Area fraction of AMH (%)
50
40
30
20
10
0
***
n.s.
hmds
hmds 4/37°C
CPD
(d)
AMH diameter (µm)
0,8
0,7
0,6
0,5
0,4
0,3
0,2
***
***
n.s.
hmds1
hmds10
hmds25
hmds50

Figure 2

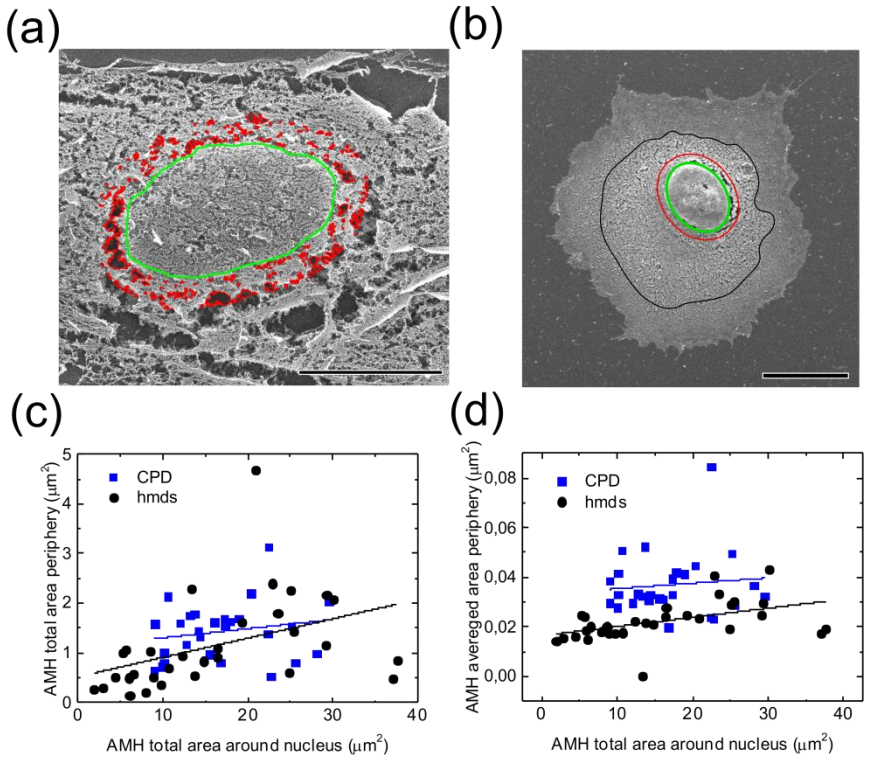
(a)
(b)
(c)
(d)
CPD
hmds
AMH total area periphery (μm²)
AMH total area around nucleus (μm²)
AMH avereged area periphery (μm²)
0
1
2
3
4
5
0,00
0,02
0,04
0,06
0,08
10
20
30
40

Figure 3

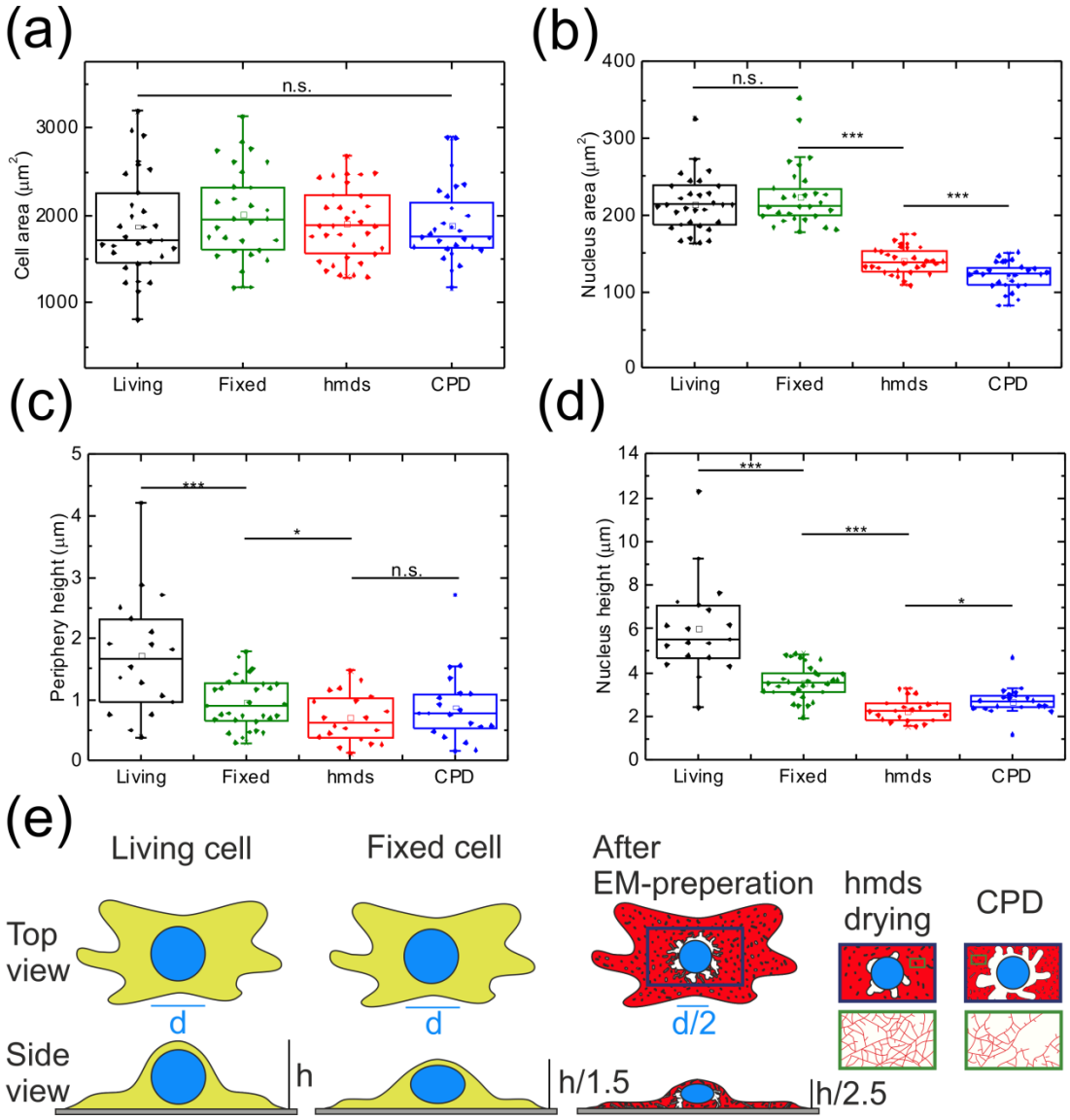
(a)
Cell area (µm²)
n.s.
Living
Fixed
hmds
CPD
(b)
Nucleus area (µm²)
n.s.
***
***
(c)
Periphery height (µm)
***
*
n.s.
(d)
Nucleus height (µm)
***
***
*
(e)
Living cell
Fixed cell
After EM-preperation
hmds drying
CPD
Top view
Side view
d
d
d/2
h
h/1.5
h/2.5

Figure 4

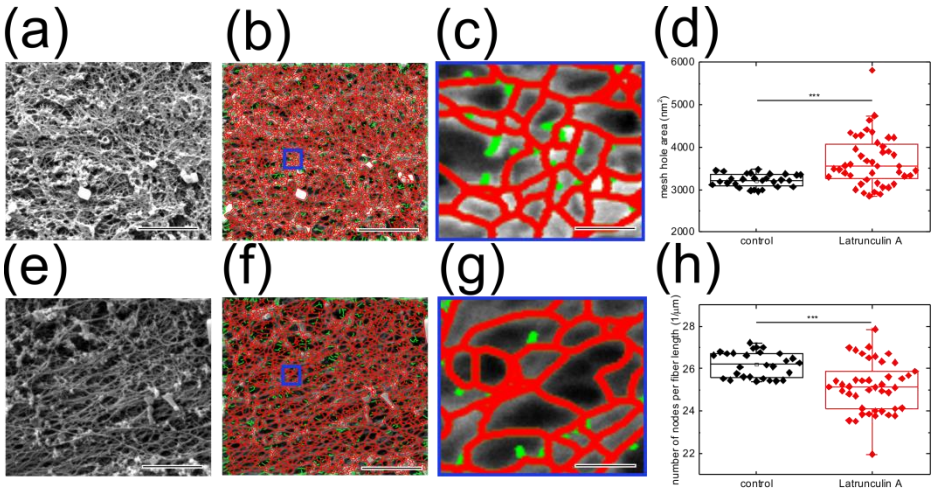
(a)
(b)
(c)
(d)
6000
5000
4000
3000
2000
mesh hole area (nm²)
***
control
Latrunculin A
(e)
(f)
(g)
(h)
28
26
24
22
number of nodes per fiber length (1/µm)
***
control
Latrunculin A

Figure 5

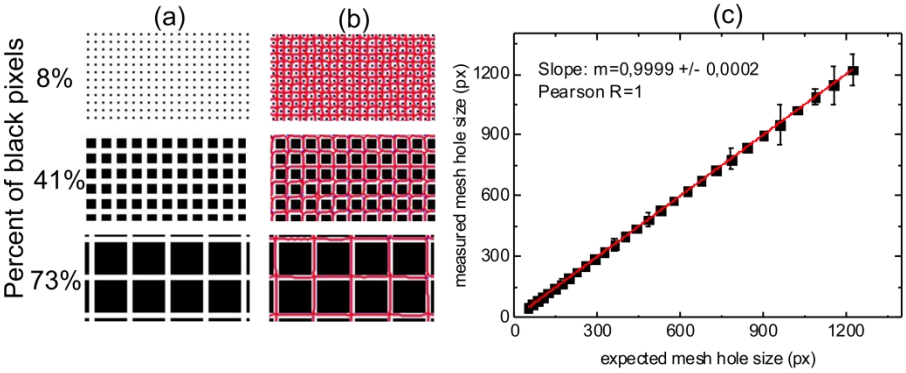
(a)
(b)
(c)
Percent of black pixels
8%
41%
73%
Slope: m=0,9999 +/- 0,0002
Pearson R=1
measured mesh hole size (px)
expected mesh hole size (px)
0
300
600
900
1200

Figure 6

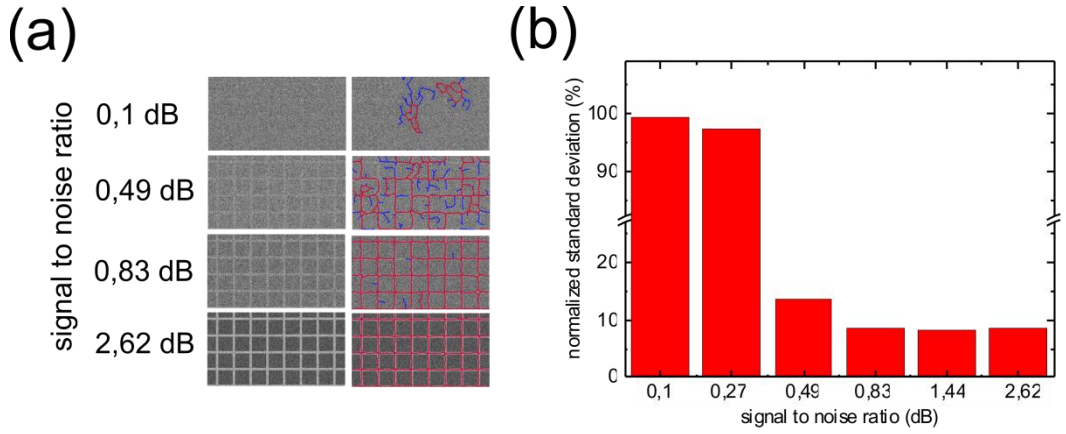
(a)
signal to noise ratio
0,1 dB
0,49 dB
0,83 dB
2,62 dB
(b)
normalized standard deviation (%)
100
90
20
10
0
0,1
0,27
0,49
0,83
1,44
2,62
signal to noise ratio (dB)

Figure 7

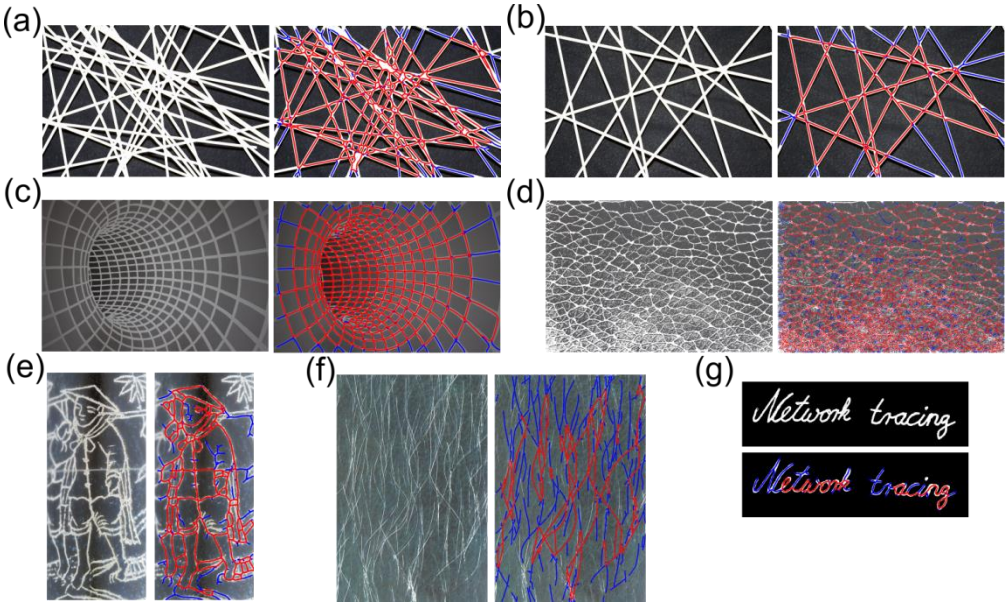

Figure 8